IEEE Access
Multidisciplinary | Rapid Review | Open Access Journal

Received September 27, 2021, accepted October 29, 2021, date of publication November 11, 2021,
date of current version November 22, 2021.

Digital Object Identifier 10.1109/ACCESS.2021.3127575

MIMO H_∞ Feedback Controller With Feedforward Compensator for Scanning Tunneling Microscope Having 3D Cross-Coupled Piezoelectric Actuator

IRFAN AHMAD, AMRO EMAD AWAD ALI, AND YASSER BIN SALAMAH
Department of Electrical Engineering, College of Engineering, King Saud University, Riyadh 11451, Saudi Arabia

Corresponding author: Irfan Ahmad (irfahmad@ksu.edu.sa)

This work was supported by King Saud University, Riyadh, Saudi Arabia, under Researchers Supporting Project RSP-2021/270.

ABSTRACT Scanning Tunneling Microscope (STM) is used to generate the surface image of any conducting sample surface with an atomic-scale resolution. A multi-axis 3D piezoelectric actuator is attached with the STM tip to move it in horizontal (x and y) and vertical (z) directions. The purpose of control design is to achieve precise reference tracking for horizontal 2D scanning system and to keep the tunneling current constant in the vertical direction in the presence of all possible disturbances. A usual practice is to design independent single-input-single-output (SISO) controllers for individual x, y and z axes by neglecting the cross-coupling dynamics of the multi-axis 3D piezoelectric actuator. In this paper, a complete 3D STM system, without neglecting the cross-coupling dynamics as well as the hysteresis nonlinearity of the actuator, is first mathematically modeled. The parameters of the hysteresis model are identified from the real-time experimental data by using the nonlinear least-squares curve fitting problem. A feedforward compensator is then designed without finding an inverse hysteresis model to avoid any inverse modeling complexity. Then, two control strategies (SISO and multi-input-multi-output (MIMO) H_∞ feedback controllers cascaded in series with the feedforward compensator) are investigated for an overall 3D system. Three different scanning trajectories (raster, spiral and Lissajous) are considered to analyze and compare the performance of SISO and MIMO control schemes. In the presence of cross-couplings, an average improvement of 83% in reducing the variations of the tunneling current is achieved with the suggested MIMO control scheme as compared to the generally used SISO control scheme for STM.

INDEX TERMS Cross-coupling, feedforward compensator, hysteresis, MIMO H_∞ feedback controller, scanning tunneling microscope.

I. INTRODUCTION

Scanning Tunneling Microscope (STM) was invented in early 1980s by Gerd Binnig and Heinrich Rohrer [1] and they received Noble prize in physics in 1986. This great invention of STM has brought about a revolution in the field of nanotechnology due to its capability of scanning the conducting surfaces with an atomic-scale resolution. STM operation is based on a quantum mechanical phenomenon of the tunneling current which was first noticed in 1927 by Friedrich Hund [2]. Briefly, if two conducting materials (a sharp metallic tip and a conducting sample surface in case of STM) are brought near to each other so that the distance between them is from $0.1 - 1 \times 10^{-9}$ m and a bias voltage is applied between them, then a potential barrier is overcome by the electrons and they tunnel through the vacuum creating a sensitive current named *tunneling current*. An important application of the tunneling current is to characterize the surface morphology with an atomic-scale resolution through STM. Other applications of the tunneling current are to measure the accelerations down to sub-micro-g [3], [4] and to sense sub-micrometer displacements [5], [6].

Tunneling current is highly sensitive to the distance between the tip and the sample surface. In STM, the objective

The associate editor coordinating the review of this manuscript and approving it for publication was Hui Xie.

is to keep the tunneling current constant (vertical z-direction) while scanning the sample surface (horizontal x-y directions) to generate its topographical image with an atomic-scale resolution. When the distance between the tip and the sample surface increases or decreases due to the variations in the sample topography, the control signal regulates this distance by actuating the tip away from or near to the sample surface in the vertical z-direction. The 3D displacements over the sample surface are viable by employing the multi-axis 3D piezoelectric actuator due to its capability of expanding and contracting when a voltage is applied. However, these actuators introduce some challenges from control systems point of view, such as hysteresis, creep, cross-coupling and structural vibrations [7]. These issues must be considered at the time of control design in order to achieve the desired performance of STM. If these issues are not considered then large variations in the tunneling current may result in a surface topographic image that does not correspond to the reality [8].

For the horizontal 2D scanning system of STM, the requirement is to achieve the precise reference tracking. A lot of research work has been done in this direction to control the positioning from the piezoelectric actuators for different micro - nanopositioning applications [9]–[12]. The main challenges in order to achieve the precise reference tracking are the actuator nonlinearities (e.g. hysteresis and creep) and high frequency vibrations [13]. In order to analyze the inherent hysteresis nonlinearity of the piezoelectric actuator, a number of hysteresis models are investigated in the literature [14]–[17] and accordingly, their compensation techniques are also discussed [18]–[22]. However, a commonly used compensation technique is to design an inverse hysteresis model, as a feedforward compensator, which is often a challenging task due to inverse modeling complexity. [23] can be consulted for a survey on different hysteresis models and their compensation techniques. As far as creep nonlinearity is concerned, its effects are visible only when the tracking is required over extended periods of time during slow-speed operations. A number of mathematical models for creep nonlinearity and compensation techniques are investigated in the literature [24]–[26]. However, the effects of creep nonlinearity can be neglected if the tracking is performed for a short duration of time. The issue of vibrations when tracking is performed at a high frequency is also analyzed in the literature [27]–[29]. In short, a lot of research work has already been done in order to achieve the precise reference tracking but this much effort, from control design point of view, has not been done yet to the control of piezoelectric actuator in the presence of nonlinear tunneling phenomenon (e.g. control design for the vertical tunneling current system in STM).

In most commercial equipment of STM, still the very classical proportional-integral (PI) or sometimes proportional-integral-derivative (PID) controllers are implemented for the vertical tunneling current system. The parameters of these classical controllers are adjusted manually by the operators of STM. Due to the manual adjustment of the controller parameters, there is always a high risk of achieving a surface topographic image that does not correspond to the reality. The analysis of the vertical tunneling current system of STM with classical PI controller is presented in [30]–[32]. Closed-loop stability analysis of STM with a classical PI controller to reduce the risk of tip-sample collision is presented in [33]. A variable structure control design methodology with a classical PI controller is investigated in [34] to avoid the tip-sample collision due to any sudden change in the topography of the sample surface.

As mentioned earlier, the main objective for the vertical tunneling current system is to keep the tunneling current constant while scanning the sample surface. Other than sample surface variations and the sensor noise, the cross-coupling of the multi-axis piezoelectric actuator is also an important source of producing large variations in the tunneling current. The adverse effect of cross-coupling for the vertical tunneling current system is often neglected and independent single-input-single-output (SISO) controllers are designed for individual axis of STM. Few control approaches have been investigated in the literature to compensate the cross-coupling effects in different scanning probe microscopy (SPM) applications. In [35], an inversion based iterative SISO control methodology is suggested to compensate for the x-to-z cross-coupling effect in piezo-scanners for the application of atomic force microscope (AFM). [36] further enhanced this work by using the same inversion based iterative control law to obtain the control input which is augmented, as a feedforward control, to the classical PID feedback control to cancel the cross-coupling effect in tapping-mode imaging of AFM. In [37], a SISO H_∞ feedback controller is suggested to compensate the x-to-y cross-couplings in AFM. A modified repetitive control based cross-coupling compensation approach is suggested in [38] to minimize the coupling effect in XY piezoelectric tube scanner in AFM. An internal reference model-based optimal SISO linear quadratic Gaussian (LQG) controller with a vibration compensator is suggested in [39] to compensate the cross-couplings in AFM. It has been mentioned in [7] that the cross-coupling effects in piezoelectric tube scanners must also be investigated with different MIMO control schemes. [40] has analyzed a MIMO linear quadratic integral control with Kalman observer for STM having x/y to z cross-couplings for the application of surface reconstruction. However, the cross-coupling between x and y axes of the piezoelectric actuator is neglected. A multivariable compensation technique is suggested in [41] to reduce the cross-couplings of the multi-axis 2D piezoelectric actuator.

It has been observed by the authors of this paper that mostly SISO control methodologies are investigated to compensate the cross-coupling in different SPM applications and most of this work is related to AFM. There is a scarcity of research work about the compensation of cross-couplings through some advanced control design in STM. The idea of the presented work is to analyze the performance of STM by

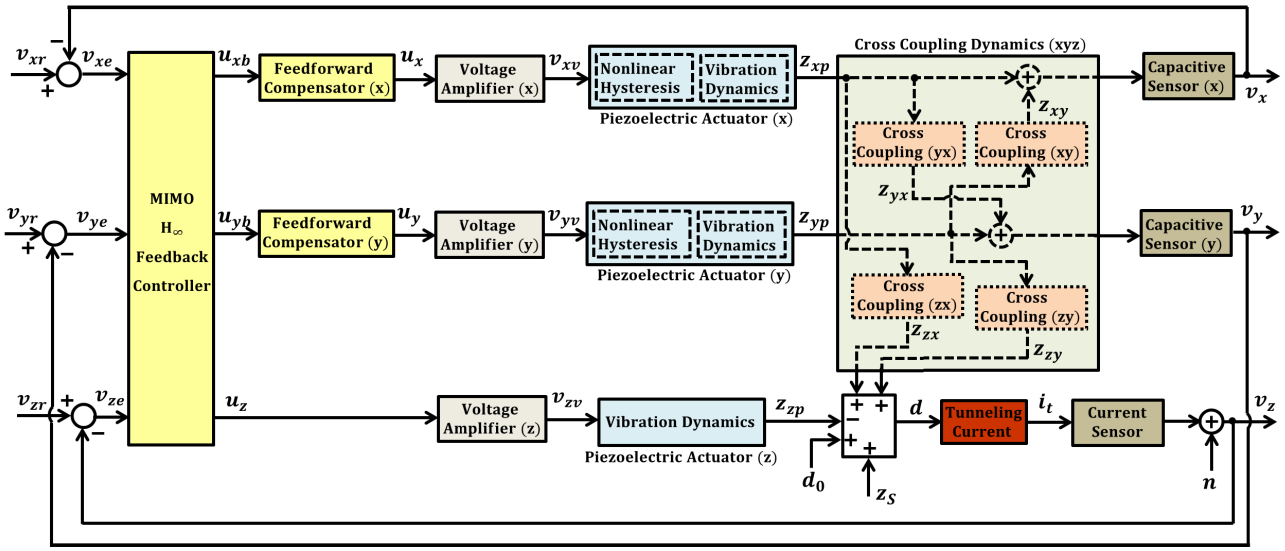

FIGURE 1. Block diagram of 3D Scanning Tunneling Microscope with cross-couplings and the suggested feedback / feedforward control scheme.

considering not only the cross coupling dynamics of the multi-axis 3D piezoelectric actuator and its effect on all 3 axes of the system but also the nonlinear hysteresis phenomenon of the actuator. It is always an interesting study to consider the different adverse effects, which can degrade the performance of the considered system, altogether. Cross-couplings and hysteresis are the two most significant undesirable behaviors of the multi-axis piezoelectric actuator which can not be neglected. To deal with both of these issues, a MIMO H_∞ feedback controller cascaded in series with a feedforward compensator is thoroughly analyzed in this paper in order to achieve the precise reference tracking for a 2D horizontal scanning system and to keep the tunneling current constant in the vertical z-direction, while scanning the sample surface.

The main contributions of this paper are:

- A complete 3D MIMO system of STM, by considering the cross-couplings dynamics as well as the hysteresis nonlinearity of the multi-axis piezoelectric actuator, is mathematically modeled.
- The parameters of the hysteresis model are identified from the real-time experimental data and the hysteresis compensator is designed without formulating an inverse hysteresis model to avoid inverse modeling complexity.
- In contrast to the usual practice of designing independent SISO controllers for individual axis of STM, MIMO H_∞ feedback controller cascaded in series with the feedforward compensator is suggested and thoroughly analyzed.
- The performance of the suggested MIMO control scheme is compared with the SISO control scheme by analyzing three different scanning trajectories (raster scanning, spiral scanning and Lissajous scanning).

This manuscript is organized as follows: *Section II* presents the working principle of STM. Mathematical modeling of the considered MIMO system, having a horizontal scanning system with hysteresis nonlinearity, cross-coupling dynamics and a vertical tunneling current system, is presented in *Section III*. *Section IV* discusses in detail about the controller design. This section starts with the formulation of the control problem and expresses the desired performance of the system. Then, feedforward compensator design and MIMO H_∞ feedback controller design schemes are presented in this section. *Section V* presents the achieved results of the horizontal scanning system as well as the tunneling current system by considering raster, spiral and Lissajous scanning. Finally, *Section VI* concludes this paper.

II. WORKING PRINCIPLE OF SCANNING TUNNELING MICROSCOPE

STM consists of a 2D horizontal scanning system in x and y directions and a 1D vertical tunneling current system in z direction. Overall, the block diagram of the considered 3D STM system with the suggested MIMO control strategy is shown in Fig. 1.

The working principle of STM is first to bring the sharp metallic tip, attached with a piezoelectric actuator, in the tunneling region so that the distance (d) between the tip and the conducting sample surface must be less than 1×10^{-9} m. When the sharp metallic tip comes in the tunneling region to scan the sample surface, a bias voltage applied between the two allows the electrons to tunnel through the vacuum separating them. The direction of the resulting tunneling current (i_t) depends on the polarity of the applied bias voltage. The purpose of control design for STM is to achieve the precise reference tracking for a 2D horizontal scanning system (in x and y directions) and to keep the tunneling current constant in the vertical z-direction in the presence of all possible disturbances. The control signal which keeps the tunneling current constant in the vertical z-direction helps to generate the topographic image of the sample surface with an atomic-scale resolution. A mutli-axis 3D piezoelectric

actuator moves the tip in the appropriate direction depending on the applied voltages (v_{xv} and v_{yv} for the horizontal displacement in x and y directions respectively and v_{zv} for the vertical displacement in z-direction) given by the voltage amplifier. The input voltages (u_x, u_y and u_z) of the voltage amplifier are adjusted by the controller.

For a 2D horizontal scanning system, the output displacements (z_{xp} and z_{yp} in x and y directions respectively) of the piezoelectric actuator are perturbed due to cross-couplings among these two axes. Coupling-caused positioning errors (z_{xy} and z_{yx}) will be added in the actual displacements (z_{xp} and z_{yp}) of the actuator and these overall displacements are sensed by the capacitive position sensors. These position sensors generate the output voltages (v_x and v_y) which are used for the feedback. The feedback voltages are compared with the reference voltages (v_{xr} and v_{yr} for x and y directions respectively) to generate the error voltages (v_{xe} and v_{ye}). For a 2D horizontal scanning system, the piezoelectric actuator consists of linear vibration dynamics as well as the nonlinear hysteresis phenomenon. The nonlinear hysteresis behavior is modeled for the horizontal scanning system as the displacements in x and y directions are in micro-scale. However, the nonlinear hysteresis behavior of the piezoelectric actuator is neglected for the vertical displacement in z-direction as the overall displacement is in sub-nano scale. The cross-coupling effect due to sub-nano scale displacement in z direction on the other two axes (x and y) can also be neglected.

For the vertical tunneling current system, the actual output displacement (z_{zp}) of the piezoelectric actuator is perturbed due coupling-caused positioning errors (z_{zx} and z_{zy} due to displacements in x and y directions respectively). Other than this overall displacement of the piezoelectric actuator, the sample surface variations (z_S) changes the distance (d) between the tip and the sample surface. Tunneling current (i_t) exponentially depends on this distance (d). Changes in distance (d) while scanning the sample surface bring changes in the tunneling current (i_t). The current sensor, which measures the tunneling current, is a current to voltage converter with a high gain. It converts the weak tunneling current (i_t) in nano-amperes into a voltage. Measurement noise (n) induces variations in the measured tunneling voltage (v_z). This tunneling voltage (v_z) is then compared with the reference input voltage (v_{zr}) which corresponds to the desired value of the tunneling current.

In the suggested control scheme, a MIMO H_∞ feedback controller acts on the three error voltages (v_{xe}, v_{ye} and v_{ze}) and generates the control signals (u_{xb}, u_{yb} and u_z). For a 2D horizontal scanning system, the feedforward compensators are also designed for x and y axes to compensate the hysteresis nonlinearity of the actuator and cascaded in series with the feedback controller.

III. MODELING OF SCANNING TUNNELING MICROSCOPE

STM has a 2D (xy) horizontal scanning system and a vertical (z) tunneling current system. The overall 3D system is coupled with each other due to cross-couplings of the piezoelectric actuator as presented in Fig. 1. The overall mathematical model of STM is presented in this section.

A. DYNAMICS OF HORIZONTAL XY SCANNING SYSTEM

The horizontal 2D scanning system consists of a voltage amplifier, piezoelectric actuator and a capacitive position sensor. The dynamics in horizontal x-direction is considered the same as in y-direction. Therefore, 5^{th} order mathematical model of horizontal x-direction is presented here only. The same mathematical model is considered for the horizontal y-direction.

The considered state-space mathematical model of the voltage amplifier is:

$$\begin{aligned} \dot{x}_1(t) &= -\omega_{xv} \cdot x_1(t) + G_{xv}\omega_{xv} \cdot u_x(t) \\ v_{xv}(t) &= x_1(t) \end{aligned} \tag{1}$$

where, u_x and v_{xv} are input and output voltages of the voltage amplifier respectively, ω_{xv} the bandwidth and G_{xv} is the gain of the amplifier.

Piezoelectric actuator has linear dynamics as well as the hysteresis nonlinearity. The nonlinear hysteresis phenomenon of the piezoelectric actuator is modeled by considering the Bouc-Wen hysteresis model. All the necessary details about the Bouc-Wen hysteresis model can be found in [42], [43]. The reason for selecting the Bouc-Wen hysteresis model is its simplicity in representing a large class of hysteresis with accuracy, easy in implementation as well as in identification of its parameters. The hysteresis nonlinearity of the considered piezoelectric actuator is modeled as:

$$\begin{aligned} \dot{x}_2(t) &= \Gamma \dot{v}_{xv}(t) - \Phi \mid \dot{v}_{xv}(t) \mid x_2(t) - \Psi \dot{v}_{xv}(t) \mid x_2(t) \mid \\ v_{xp}(t) &= G_h v_{xv}(t) - x_2(t) \end{aligned} \tag{2}$$

where, v_{xv} and v_{xp} are input and output of the hysteresis model and Γ, Φ and Ψ are the constant parameters which govern the shape of the hysteresis loop. G_h is the coefficient of the piezoelectric actuator and is always positive. The linear dynamics of the piezoelectric actuator is represented by the following state-space model:

$$\begin{aligned} \dot{x}_3(t) &= x_4(t) \\ \dot{x}_4(t) &= -\omega_{xp}^2 \cdot x_3(t) - 2\zeta_{xp}\omega_{xp} \cdot x_4(t) + G_{xp}\omega_{xp}^2 \cdot v_{xp}(t) \\ z_{xp}(t) &= x_3(t) \end{aligned} \tag{3}$$

where, v_{xp} and z_{xp} are input voltage and output displacement of the piezoelectric actuator respectively, ω_{xp} the bandwidth, ζ_{xp} the damping coefficient and G_{xp} is the gain of the piezoelectric actuator.

The output displacement of the piezoelectric actuator is sensed by a capacitive position sensor. The output displacement of the piezoelectric actuator in x-direction (z_{xp}) is disturbed due to its cross-coupling with the displacement in y-direction. The state-space mathematical model of the capacitive position sensor is:

$$\begin{aligned} \dot{x}_5(t) &= -\omega_{xc} \cdot x_5(t) + G_{xc}\omega_{xc} \left(z_{xp}(t) + z_{xy}(t)\right) \\ v_x(t) &= x_5(t) \end{aligned} \tag{4}$$

where, v_x is output voltage of the capacitive sensor, z_{xy} is coupling-caused displacement in x-direction due to displacement in y-direction, ω_{xc} the bandwidth and G_{xc} is the gain of the capacitive position sensor.

So, the horizontal scanning system in x-direction has an overall 5^{th} order mathematical model with input and output voltages of u_x and v_x respectively. Similarly, the horizontal scanning system in y-direction has the similar 5^{th} order mathematical model with input and output voltages of u_y and v_y respectively.

B. DYNAMICS OF CROSS-COUPLING

The displacement of STM tip in x, y and z-directions are coupled with each other due to cross-couplings of the piezoelectric actuator. A number of studies have been undertaken by the research community to understand the mechanism and root causes of this unwanted behavior of the piezoelectric actuator in micro/nanopositioning stages. The primary root cause highlighted by [44] is the combination of the slip and rotation of the piezoelectric disks due to their frictional behavior, concurrent with changes in the geometry of the stage. According to [28], there are several complex reasons for the erroneous motion due to cross-couplings in the piezo-actuated micro/nanopositioning stages; for instance, the eccentricity of the scanner due to improper machining, non-uniformity of the electric field across the scanner and also the error in the orthogonality of the scanning axes due to collocated structure of the scanner.

The coupling-caused displacement in one direction, let's say in y-direction, due to the displacement in other direction, let's say in x-direction, becomes more significant when the displacement in x-direction is for large range or with high speed. The coupling-caused displacement in one direction becomes insignificant when the displacement in other direction is for small range or with slow speed. This motivates to consider the dynamics of the commonly used high-pass filter as the dynamics of the cross-coupling. As in z-direction, STM tip just needs to maintain a constant distance between the tip and the sample surface, or in order words, needs to maintain a constant tunneling current, therefore the coupling-caused displacement in other directions due to the displacement in z-direction can be neglected.

The coupling-caused displacement (z_{xy}) in x-direction due to the displacement in y-direction (z_{yp}) is represented by the following model:

$$\begin{aligned} \dot{x}_{11}(t) &= -\omega_{cc} \cdot x_{11}(t) + z_{yp}(t) \\ z_{xy}(t) &= G_{cc}\omega_{cc} \cdot x_{11}(t) + G_{cc} \cdot z_{yp}(t) \end{aligned} \tag{5}$$

The coupling-caused displacement (z_{yx}) in y-direction due to the displacement in x-direction (z_{xp}) is represented by the following model:

$$\begin{aligned} \dot{x}_{12}(t) &= -\omega_{cc} \cdot x_{12}(t) + z_{xp}(t) \\ z_{yx}(t) &= G_{cc}\omega_{cc} \cdot x_{12}(t) + G_{cc} \cdot z_{xp}(t) \end{aligned} \tag{6}$$

The coupling-caused displacement (z_{zx}) in z-direction due to the displacement in x-direction (z_{xp}) is represented by the following model:

$$\begin{aligned} \dot{x}_{13}(t) &= -\omega_{cc} \cdot x_{13}(t) + z_{yp}(t) \\ z_{zy}(t) &= G_{cc}\omega_{cc} \cdot x_{13}(t) + G_{cc} \cdot z_{yp}(t) \end{aligned} \tag{7}$$

The coupling-caused displacement (z_{zy}) in z-direction due to the displacement in y-direction (z_{yp}) is represented by the following model:

$$\begin{aligned} \dot{x}_{14}(t) &= -\omega_{cc} \cdot x_{14}(t) + z_{xp}(t) \\ z_{zx}(t) &= G_{cc}\omega_{cc} \cdot x_{14}(t) + G_{cc} \cdot z_{xp}(t) \end{aligned} \tag{8}$$

Here, in (5)-(8), G_{cc} is the gain which represents the maximum coupling-caused positioning error and ω_{cc} is the bandwidth of the high pass filter which represents the scanning speed.

C. DYNAMICS OF VERTICAL Z TUNNELING CURRENT SYSTEM

The vertical z tunneling current system consists of a voltage amplifier, piezoelectric actuator for the precise movement of the tip in vertical z-direction and a current sensor for the measurement of tunneling current.

The voltage amplifier is modeled as:

$$\begin{aligned} \dot{x}_{15}(t) &= -\omega_{zv} \cdot x_{15}(t) + G_{zv}\omega_{zv} \cdot u_z(t) \\ v_{zv}(t) &= x_{15}(t) \end{aligned} \tag{9}$$

where, u_z and v_{zv} are input and output voltages of the voltage amplifier respectively, ω_{zv} the bandwidth and G_{zv} is the gain of the amplifier.

The movement of STM tip in the vertical z-direction is in sub-nano scale, therefore, 2^{nd} order linear dynamics is considered for the piezoelectric actuator and hysteresis nonlinearity of the actuator in neglected. The considered mathematical model of the piezoelectric actuator is:

$$\begin{aligned} \dot{x}_{16}(t) &= x_{17}(t) \\ \dot{x}_{17}(t) &= -\omega_{zp}^2 \cdot x_{16}(t) - 2\zeta_{zp}\omega_{zp} \cdot x_{17}(t) + G_{zp}\omega_{zp}^2 \cdot v_{zp}(t) \\ z_{zp}(t) &= x_{16}(t) \end{aligned} \tag{10}$$

where, v_{zp} and z_{zp} are input voltage and output displacement of the piezoelectric actuator respectively, ω_{zp} the bandwidth, ζ_{zp} the damping coefficient and G_{zp} is the gain of the piezoelectric actuator.

The tunneling current (i_t) depends exponentially on the distance (d) between the tip and the sample surface. This distance can be obtained as:

$$d(t) = d_0 + z_S(t) + z_{zx}(t) + z_{zy}(t) - z_{zp}(t) \tag{11}$$

where, d_0 is the initial distance, z_S is the unknown sample surface variations, z_{zx} and z_{zy} are the coupling-caused displacements in z-direction due to the displacements in x and y-directions respectively and z_{zp} is the output displacement of the piezoelectric actuator in z-direction. The change in

distance (d) will change the tunneling current (i_t) which can be modeled by an exponential static nonlinearity as:

$$\begin{aligned} i_t(t) &= i_0 \cdot e^{-k \cdot d(t)}; \quad if\ 0 \le d(t) \le 1 \times 10^{-9} m \\ i_t(t) &= 0; \quad if\ d(t) > 1 \times 10^{-9} m \end{aligned} \tag{12}$$

where, i_0 is the initial tunneling current and k is a constant which depends on the work function of the tip and the sample surface. The tunneling current equation can be linearized by using the first-order linear approximation approach around an operating point. The linearized equation of the tunneling current is:

$$i_t(t) = i_p - k \cdot i_p \left(d(t) - d_p\right) \tag{13}$$

where, i_p and d_p are the operating points of the tunneling current and the corresponding distance between the tip and the sample surface respectively.

The current sensor measures the tunneling current and generate the corresponding voltage accordingly. The current sensor is mathematically modeled as:

$$\begin{aligned} \dot{x}_{18}(t) &= -\omega_{zc} \cdot x_{18}(t) + G_{zc}\omega_{zc} \cdot i(t) \\ v_z(t) &= x_{18}(t) + n(t) \end{aligned} \tag{14}$$

where, v_z is the output voltage of the sensor, ω_{zc} the bandwidth, G_{zc} the gain and n is the measurement noise.

So, the vertical tunneling current system has an overall 4^{th} order mathematical model with input and output voltages of u_z and v_z respectively.

D. OVERALL DYNAMICS OF MIMO SYSTEM

The overall dynamics of the considered MIMO system has three inputs (u_x, u_y and u_z) and three outputs (v_x, v_y and v_z). This overall dynamics of a 3D MIMO system can be represented as:

$$\begin{aligned}
\dot{x}_1(t) &= -\omega_{xv} \cdot x_1(t) + G_{xv}\omega_{xv} \cdot u_x(t) \\
\dot{x}_2(t) &= \Gamma \dot{x}_1(t) - \Phi \mid \dot{x}_1(t) \mid x_2(t) - \Psi \dot{x}_1(t) \mid x_2(t) \mid \\
\dot{x}_3(t) &= x_4(t) \\
\dot{x}_4(t) &= G_{xp}G_h\omega_{xp}^2 \cdot x_1(t) - G_{xp}\omega_{xp}^2 \cdot x_2(t) - \omega_{xp}^2 \cdot x_3(t) \\
&\quad -2\zeta_{xp}\omega_{xp} \cdot x_4(t) \\
\dot{x}_5(t) &= G_{xc}\omega_{xc} \cdot x_3(t) - \omega_{xc} \cdot x_5(t) + G_{xc}G_{cc}\omega_{xc} \cdot x_8(t) \\
&\quad +G_{xc}G_{cc}\omega_{xc}\omega_{cc} \cdot x_{11}(t) \\
\dot{x}_6(t) &= -\omega_{yv} \cdot x_6(t) + G_{yv}\omega_{yv} \cdot u_y(t) \\
\dot{x}_7(t) &= \Gamma \dot{x}_6(t) - \Phi \mid \dot{x}_6(t) \mid x_7(t) - \Psi \dot{x}_6(t) \mid x_7(t) \mid \\
\dot{x}_8(t) &= x_9(t) \\
\dot{x}_9(t) &= G_{yp}G_h\omega_{yp}^2 \cdot x_6(t) - G_{yp}\omega_{yp}^2 \cdot x_7(t) - \omega_{yp}^2 \cdot x_8(t) \\
&\quad -2\zeta_{yp}\omega_{yp} \cdot x_9(t) \\
\dot{x}_{10}(t) &= G_{yc}G_{cc}\omega_{yc} \cdot x_3(t) + G_{yc}\omega_{yc} \cdot x_8(t) - \omega_{yc} \cdot x_{10}(t) \\
&\quad +G_{yc}G_{cc}\omega_{yc}\omega_{cc} \cdot x_{12}(t) \\
\dot{x}_{11}(t) &= x_8(t) - \omega_{cc} \cdot x_{11}(t) \\
\dot{x}_{12}(t) &= x_3(t) - \omega_{cc} \cdot x_{12}(t) \\
\dot{x}_{13}(t) &= x_8(t) - \omega_{cc} \cdot x_{13}(t) \\
\dot{x}_{14}(t) &= x_3(t) - \omega_{cc} \cdot x_{14}(t) \\
\dot{x}_{15}(t) &= -\omega_{zv} \cdot x_{15}(t) + G_{zv}\omega_{zv} \cdot u_z(t) \\
\dot{x}_{16}(t) &= x_{17}(t) \\
\dot{x}_{17}(t) &= G_{zp}\omega_{zp}^2 \cdot x_{15}(t) - \omega_{zp}^2 \cdot x_{16}(t) - 2\zeta_{zp}\omega_{zp} \cdot x_{17}(t) \\
\dot{x}_{18}(t) &= -kG_{zc}G_{cc}\omega_{zc}i_p \cdot (x_3(t) + x_8(t)) - \omega_{zc} \cdot x_{18}(t) \\
&\quad -kG_{zc}G_{cc}\omega_{zc}\omega_{cc}i_p \cdot (x_{13}(t) + x_{14}(t)) \\
&\quad +kG_{zc}\omega_{zc}i_p \cdot x_{16}(t) - kG_{zc}\omega_{zc}i_p \cdot z_S(t) \\
v_x(t) &= x_5(t) \\
v_y(t) &= x_{10}(t) \\
v_z(t) &= x_{18}(t) + n(t)
\end{aligned} \tag{15}$$

All parameter of the above MIMO model are defined earlier and their values are given in Table 1.

TABLE 1. Parameter values of 3D Scanning Tunneling Microscope.

Description	Parameters	Value	Axis
Bandwidth of voltage amplifier	$\omega_{xv}, \omega_{yv}, \omega_{zv}$	4 kHz	x,y,z
Gain of voltage amplifier	G_{xv}, G_{yv}, G_{zv}	15	x,y,z
Bandwidth of piezoelectric actuator	ω_{xp}, ω_{yp}	630 Hz	x,y
	ω_{zp}	120 kHz	z
Gain of piezoelectric actuator	G_{xp}, G_{yp}	235 nm/V	x,y
	G_{zp}	1.2 nm/V	z
Damping of piezoelectric actuator	$\zeta_{xp}, \zeta_{yp}, \zeta_{zp}$	0.7	x,y,z
Bandwidth of position sensor	ω_{xc}, ω_{yc}	8.5 kHz	x,y
Gain of position sensor	G_{xc}, G_{yc}	200 V/mm	x,y
Bandwidth of current sensor	ω_{zc}	13 kHz	z
Gain of current sensor	G_{zc}	10^9 V/A	z
Tunneling current constant	k	1.65 $Å^{-1}$	z
Operating pt. of tunneling current	i_p	0.5 nA	z
Max. scan speed for cross-coupling	ω_{cc}	10 Hz	x,y
Maximum coupling-caused positioning error (% of scanning displacement)	G_{cc}	3%	x,y

IV. CONTROLLER DESIGN

In this section, first of all, the control problem and the desired performance of STM is highlighted. Then, in order to achieve the desired performance, the feedforward compensator as well as the MIMO H_∞ feedback control design schemes are presented.

A. CONTROL PROBLEM AND DESIRED PERFORMANCE

The objective of control design for STM, when its tip moves in 3-directions (x, y and z), is to achieve the precise reference tracking in x and y-directions in order to scan the sample surface and also to maintain the tunneling current constant, while scanning the sample surface, in the vertical z-direction. Due to the cross-couplings of the piezoelectric actuator, coupling-caused displacements in each direction (x, y or z) act as a disturbance. Other than this, sample surface variations (z_S) as well as sensor noise (n) also act as external disturbances. So, the control problem is to achieve precise

reference tracking in the horizontal (x and y) direction and also to maintain the tunneling current constant in the vertical (z) direction by rejecting the effects of all the disturbances, indeed by maintaining the closed-loop stability of the overall system.

The desired performance of STM is to achieve precise reference tracking in the horizontal (x and y) direction with mean-absolute-error of less than 1% of the reference trajectory and the maximum allowed variations of the tunneling current in the vertical (z) direction is ±5%. It means that if the reference tunneling current is 0.5nA then the maximum allowed variations of the tunneling current must be in between 0.475nA and 0.525nA while scanning the sample surface in the presence of all possible disturbances. Other than this, the initial overshoot of the tunneling current must also be less than 5% in order to avoid the collision between the sharp metallic tip and the sample surface.

B. FEEDFORWARD COMPENSATOR DESIGN

To deal with the hysteresis nonlinearity of the piezoelectric actuator, a feedforward compensator is designed. A usual practice to design a feedforward compensator is to design an inverse hysteresis model. Then, the inverse hysteresis model is usually cascaded in series with the nonlinear model of the piezoelectric actuator to compensate the hysteresis nonlinearity. Designing an inverse hysteresis model is often a challenging task due to the inverse-modeling and computational complexity.

In this paper, the feedforward compensator is designed without calculating the inverse hysteresis model, rather only the inverse of the piezoelectric coefficient is required, which is strictly positive, with the identified hysteresis model [45]. So, the first step is to identify the parameters of the considered hysteresis model (2) as well as the piezoelectric coefficient. For this purpose, an experimental setup having a single-axis all-ceramic insulated piezo-actuated micropositioning stage (P-752.21 produced by Physik Instrumente GmbH & Co.) with an integrated capacitive position sensor (D-015) is considered. The micropositioning stage is driven by a voltage amplifier (E-505) to amplify the voltage generated from a host computer and connected through a 16-bit multi-function I/O (input/output) module (PXIe-6361 produced by National Instruments). The experimental setup with micropositioning stage is shown in Fig. 2. For the real-time experimentation, a sinusoidal input voltage of 40V with a frequency of 10Hz is applied to the piezoelectric actuator. The output displacement of the piezoelectric actuator is sensed with the help of a capacitive position sensor. Then, a nonlinear curve-fitting problem is solved in a least-square sense by using the nonlinear optimization toolbox in MATLAB. The identified parameters of the considered hysteresis model (2) with piezoelectric coefficient are $\Gamma = 0.7091$, $\Phi = 2.0476$, $\Psi = 0.1949$ and $G_h = 1.143$. The experimental and simulated hysteresis loops are presented in Fig. 3(a).

To analyze the mismatch of the hysteresis loops, the experimental displacement as well as the simulated displacement

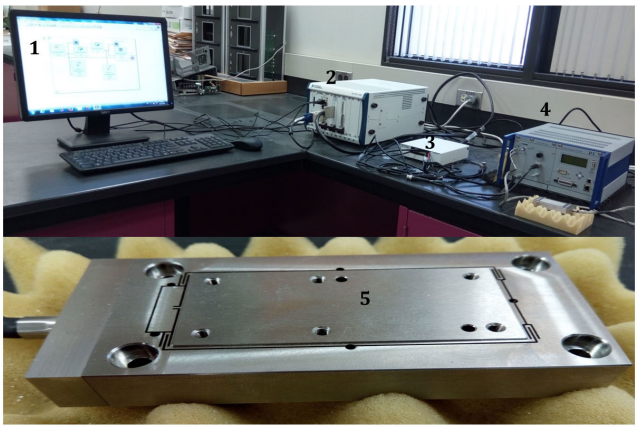

1 Host computer
2 Amplifier module (E-505)
3 I/O connector
4 Multi-function I/O module (PXIe-6361)
5 Piezo-actuated micro-nanopositioning stage (P-752.21)

FIGURE 2. Experimental setup with micro-nanopositioning stage.

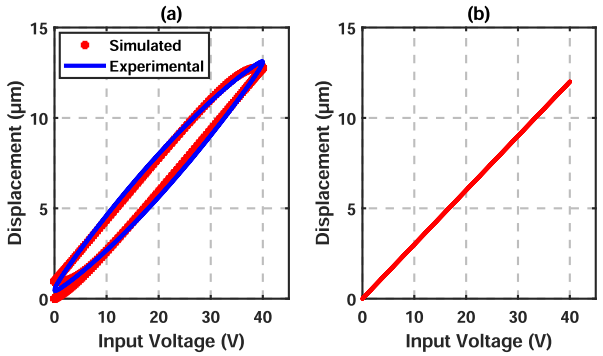

FIGURE 3. (a) Experimental and simulated hysteresis loops (b) Hysteresis loop with suggested hysteresis compensator.

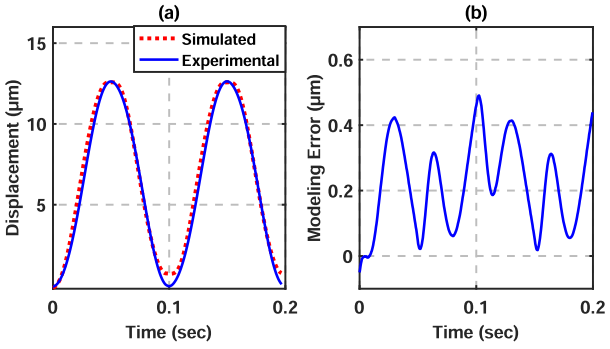

FIGURE 4. (a) Experimental and simulated displacements of piezoelectric actuator with considered hysteresis model for a sinusoidal input voltage (b) Difference between experimental and simulated displacements as modeling error.

of the piezoelectric actuator with the considered hysteresis model is presented in Fig. 4(a). A small difference between these two plots can be observed which is presented as modeling error in Fig. 4(b). It can be observed in Fig. 4(b) that the peak-to-peak modeling error is 0.48μm which is

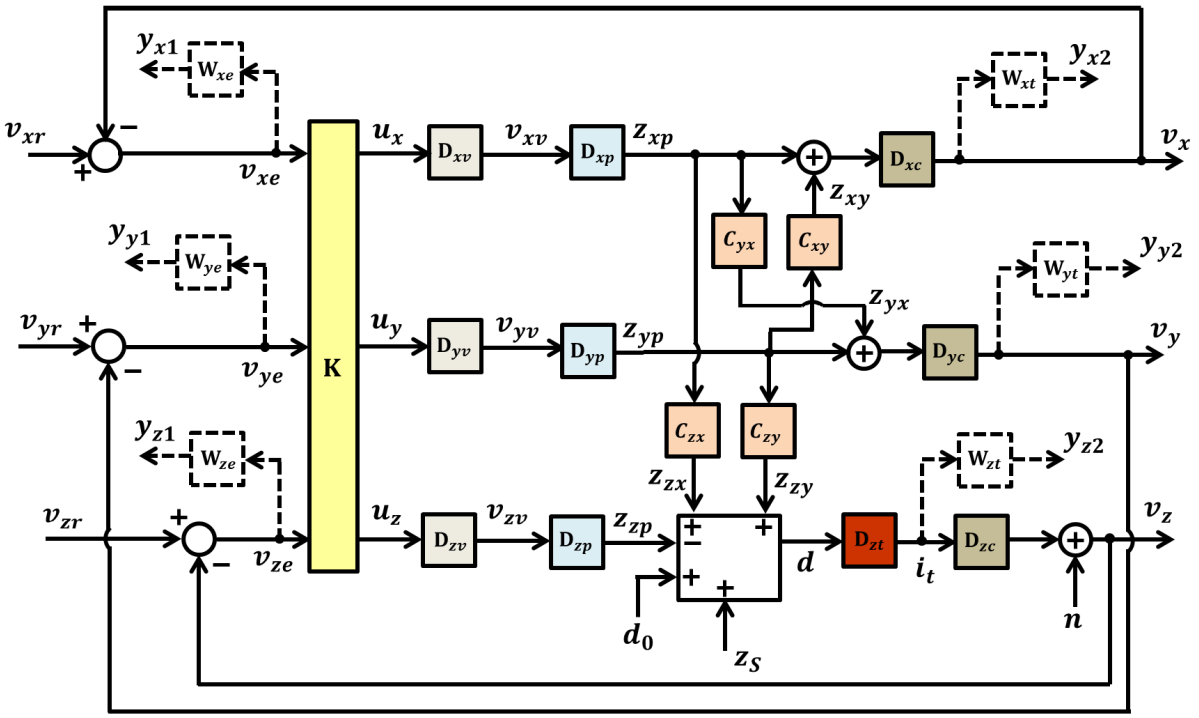

FIGURE 5. Control loop for MIMO H_∞ control design with performance weighting functions.

around 3.7% of the displacement of the piezoelectric actuator. A close match between the experimental and the simulated displacements of the piezoelectric actuator in Fig. 4(a) and also the experimental and the simulated hysteresis loops in Fig. 3(a) validate the nonlinear hysteresis model for the considered piezoelectric actuator. The modeling error will be dealt with the robustness of the suggested MIMO H_∞ feedback controller.

The feedforward compensator for the horizontal x-direction, without calculating the inverse hysteresis model, is designed as follows:

$$u_x(t) = \frac{1}{G_h}\Big(x_2(t) + u_{xb}(t)\Big) \tag{16}$$

where, u_{xb} and u_x are input and output voltages of the feedforward compensator, G_h piezoelectric coefficient and x_2 is the solution of nonlinear hysteresis model (2). It can be noticed here that there is no need to calculate the inverse of the hysteresis model for this compensator design. If this compensator is cascaded in series with the hysteresis model then the achieved result, as presented in Fig. 3(b) shows that the nonlinear hysteresis phenomenon is well compensated by the feedforward compensator. The same compensator is designed for the horizontal scanning system in y-direction. The feedforward compensator for the horizontal y-direction is designed as follows:

$$u_y(t) = \frac{1}{G_h}\Big(x_7(t) + u_{yb}(t)\Big) \tag{17}$$

where, u_{yb} and u_y are input and output voltages of the feedforward compensator in the horizontal y-direction respectively.

C. MIMO H_∞ FEEDBACK CONTROLLER DESIGN

In order to design the MIMO H_∞ feedback controller, the linearized system model is used where the hysteresis nonlinearity is well compensated by the feedforward compensator. However, after designing the feedback controller, the validation of the controller is performed in simulations in the presence of actual nonlinear system model.

The considered block diagram for the feedback controller design is presented in Fig. 5. In this block diagram, six performance weighting functions (W_{xe}, W_{xt}, W_{ye}, W_{yt}, W_{ze} and W_{zt}) can be observed which are designed in order to weight the controlled outputs y_{x1}, y_{x2}, y_{y1}, y_{y2}, y_{z1} and y_{z2} respectively. In this Fig. 5, D_{xv} (x-direction), D_{yv} (y-direction) and D_{zv} (z-direction) represent the dynamics of the voltage amplifier, D_{xp} (x-direction), D_{yp} (y-direction) and D_{zp} (z-direction) represent the dynamics of the piezoelectric actuator and D_{xc} (x-direction) and D_{yc} (y-direction) represent the dynamics of the capacitive position sensor. In vertical z-direction, D_{zc} represent the dynamics of the current sensor and D_{zt} represent the relationship between tunneling current (i_t) and distance (d). C_{xy} and C_{yx} represent the cross-coupling dynamics between horizontal x and y directions. C_{zx} represents the cross-coupling dynamics between x and z directions and C_{zy} represents between y and z directions.

The first performance weighting function (W_{xe}) is designed as follows:

$$\begin{aligned} \dot{z}_1(t) &= -\omega_{xe}\epsilon_{xe} \cdot z_1(t) + v_{xe}(t) \\ y_{x1}(t) &= \omega_{xe}\,(1 - \epsilon_{xe}/N_{xe}) \cdot z_1(t) + (1/N_{xe}) \cdot v_{xe}(t) \end{aligned} \tag{18}$$

where, for the inverse of this first performance weighting function, $\epsilon_{xe} = -75\ dB$ represents the maximum attenuation level in the low-frequency region, $\omega_{xe} = 1\ kHz$ represents the bandwidth and $N_{xe} = 6\ dB$ represents the maximum amplification in the high frequency region. This performance weighting function (W_{xe}) is imposed over the error signal (v_{xe}) in the horizontal x-direction which weights the controlled output y_{x1}. The similar first order dynamic models are chosen for the other two performance weighting functions (W_{ye} and W_{ze}). The dynamic model of the performance weighting function (W_{ye}) is given as:

$$\begin{aligned} \dot{z}_2(t) &= -\omega_{ye}\epsilon_{ye} \cdot z_2(t) + v_{ye}(t) \\ y_{y1}(t) &= \omega_{ye}\left(1 - \epsilon_{ye}/N_{ye}\right) \cdot z_2(t) + \left(1/N_{ye}\right) \cdot v_{ye}(t) \end{aligned} \quad (19)$$

where, this performance weighting function weights the controlled output y_{y1} and is imposed over the error signal (v_{ye}) with constant parameters of $\epsilon_{ye} = -75\ dB$, $\omega_{ye} = 1\ kHz$ and $N_{ye} = 6\ dB$. The dynamic model of the performance weighting function (W_{ze}) is given as:

$$\begin{aligned} \dot{z}_3(t) &= -\omega_{ze}\epsilon_{ze} \cdot z_3(t) + v_{ze}(t) \\ y_{z1}(t) &= \omega_{ze}\left(1 - \epsilon_{ze}/N_{ze}\right) \cdot z_3(t) + (1/N_{ze}) \cdot v_{ze}(t) \end{aligned} \quad (20)$$

where, this performance weighting function weights the controlled output y_{z1} and is imposed over the error signal (v_{ze}) with constant parameters of $\epsilon_{ze} = -75\ dB$, $\omega_{ze} = 3.8\ kHz$ and $N_{ze} = 6\ dB$.

The performance weighting function (W_{xt}) is designed as follows:

$$\begin{aligned} \dot{z}_4(t) &= -(\omega_{xt}/\epsilon_{xt}) \cdot z_4(t) + (1/\epsilon_{xt}) \cdot v_x(t) \\ y_{x2}(t) &= \omega_{xt}\left(1/N_{xt} - 1/\epsilon_{xt}\right) \cdot z_4(t) + (1/\epsilon_{xt}) \cdot v_x(t) \end{aligned} \quad (21)$$

where, for the inverse of this performance weighting function, $N_{xt} = 3.5\ dB$ represents the amplification in the low frequency region, $\omega_{xt} = 2\ kHz$ bandwidth and $\epsilon_{xt} = -45\ dB$ represents the maximum attenuation level in the high frequency region. The similar first order dynamic models are selected for W_{yt} and W_{zt}. The dynamic model of the performance weighting function (W_{yt}) is:

$$\begin{aligned} \dot{z}_5(t) &= -(\omega_{yt}/\epsilon_{yt}) \cdot z_5(t) + (1/\epsilon_{yt}) \cdot v_y(t) \\ y_{y2}(t) &= \omega_{yt}\left(1/N_{yt} - 1/\epsilon_{yt}\right) \cdot z_5(t) + \left(1/\epsilon_{yt}\right) \cdot v_y(t) \end{aligned} \quad (22)$$

where, $N_{yt} = 3.5\ dB$, $\omega_{yt} = 2\ kHz$ and $\epsilon_{yt} = -45\ dB$ are the constant parameters. The dynamic model of the performance weighting function (W_{zt}) is:

$$\begin{aligned} \dot{z}_6(t) &= -(\omega_{zt}/\epsilon_{zt}) \cdot z_6(t) + (1/\epsilon_{zt}) \cdot i_t(t) \\ y_{z2}(t) &= \omega_{zt}\left(1/N_{zt} - 1/\epsilon_{zt}\right) \cdot z_6(t) + (1/\epsilon_{zt}) \cdot i_t(t) \end{aligned} \quad (23)$$

where, $N_{zt} = 3.5\ dB$, $\omega_{zt} = 4\ kHz$ and $\epsilon_{zt} = -45\ dB$ are the constant parameters. W_{xt}, W_{yt} and W_{zt} weight the controlled outputs y_{x2}, y_{y2} and y_{z2} respectively as shown in Fig. 5. These values are selected in order to achieve the desired performance in terms of precise reference tracking in horizontal x and y directions, maintaining tunneling current (i_t) at the desired value in the presence of all the disturbances and to achieve good robustness and stability margins.

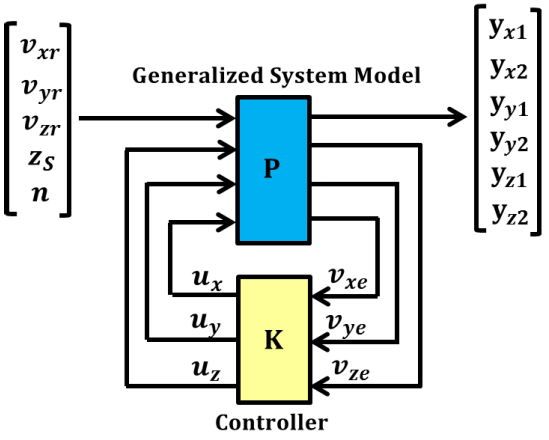

FIGURE 6. Block diagram of the generalized system model with controller.

After designing the performance weighting functions, the next step is to achieve a generalized system model (P) which is actually the combination of the overall system model with the performance weighting functions. The input vector of the generalized plant model is $[v_{xr}\ v_{yr}\ v_{zr}\ z_S\ n\ u_x\ u_y\ u_z]^T$ and the output vector is $[y_{x1}\ y_{x2}\ y_{y1}\ y_{y2}\ y_{z1}\ y_{z2}\ v_{xe}\ v_{ye}\ v_{ze}]^T$ as shown in Fig. 6. The generalized system model (P) can be described as:

$$\begin{bmatrix} y_{x1} \\ y_{x2} \\ y_{y1} \\ y_{y2} \\ y_{z1} \\ y_{z2} \\ v_{xe} \\ v_{ye} \\ v_{ze} \end{bmatrix} = \underbrace{\begin{bmatrix} P_{11} & 0 & 0 & 0 & 0 & P_{16} & P_{17} & 0 \\ 0 & 0 & 0 & 0 & 0 & P_{26} & P_{27} & 0 \\ 0 & P_{32} & 0 & 0 & 0 & P_{36} & P_{37} & 0 \\ 0 & 0 & 0 & 0 & 0 & P_{46} & P_{47} & 0 \\ 0 & 0 & P_{53} & P_{54} & P_{55} & P_{56} & P_{57} & P_{58} \\ 0 & 0 & 0 & P_{64} & 0 & P_{66} & P_{67} & P_{68} \\ 1 & 0 & 0 & 0 & 0 & P_{76} & P_{77} & 0 \\ 0 & 1 & 0 & 0 & 0 & P_{86} & P_{87} & 0 \\ 0 & 0 & 1 & P_{94} & -1 & P_{96} & P_{97} & P_{98} \end{bmatrix}}_{P} \begin{bmatrix} v_{xr} \\ v_{yr} \\ v_{zr} \\ z_S \\ n \\ u_x \\ u_y \\ u_z \end{bmatrix} \quad (24)$$

where,

$$\begin{aligned} P_{11} &= W_{xe} \\ P_{16} &= -W_{xe}D_{xv}D_{xp}D_{xc} \\ P_{17} &= -W_{xe}D_{yv}D_{yp}C_{xy}D_{xc} \\ P_{26} &= W_{xt}D_{xv}D_{xp}D_{xc} \\ P_{27} &= W_{xt}D_{yv}D_{yp}C_{xy}D_{xc} \\ P_{32} &= W_{ye} \\ P_{36} &= -W_{ye}D_{xv}D_{xp}C_{yx}D_{yc} \\ P_{37} &= -W_{ye}D_{yv}D_{yp}D_{yc} \\ P_{46} &= W_{yt}D_{xv}D_{xp}C_{yx}D_{yc} \\ P_{47} &= W_{yt}D_{yv}D_{yp}D_{yc} \\ P_{53} &= W_{ze} \\ P_{54} &= -W_{ze}D_{zt}D_{zc} \end{aligned}$$

$$
\begin{aligned}
P_{55} &= -W_{ze} \\
P_{56} &= -W_{ze}D_{xv}D_{xp}C_{zx}D_{zt}D_{zc} \\
P_{57} &= -W_{ze}D_{yv}D_{yp}C_{zy}D_{zt}D_{zc} \\
P_{58} &= W_{ze}D_{zv}D_{zp}D_{zt}D_{zc} \\
P_{64} &= W_{zt}D_{zt} \\
P_{66} &= W_{zt}D_{xv}D_{xp}C_{zx}D_{zt} \\
P_{67} &= W_{zt}D_{yv}D_{yp}C_{zy}D_{zt} \\
P_{68} &= -W_{zt}D_{zv}D_{zp}D_{zt} \\
P_{76} &= -D_{xv}D_{xp}D_{xc} \\
P_{77} &= -D_{yv}D_{yp}C_{xy}D_{xc} \\
P_{86} &= -D_{xv}D_{xp}C_{yx}D_{yc} \\
P_{87} &= -D_{yv}D_{yp}D_{yc} \\
P_{94} &= -D_{zt}D_{zc} \\
P_{96} &= -D_{xv}D_{xp}C_{zx}D_{zt}D_{zc} \\
P_{97} &= -D_{yv}D_{yp}C_{zy}D_{zt}D_{zc} \\
P_{98} &= D_{zv}D_{zp}D_{zt}D_{zc}.
\end{aligned}
$$

If $P = \begin{bmatrix} P_{up1} & P_{up2} \\ P_{lo1} & P_{lo2} \end{bmatrix}$ then:

$$
P_{up1} = \begin{bmatrix} P_{11} & 0 & 0 & 0 & 0 \\ 0 & 0 & 0 & 0 & 0 \\ 0 & P_{32} & 0 & 0 & 0 \\ 0 & 0 & 0 & 0 & 0 \\ 0 & 0 & P_{53} & P_{54} & P_{55} \\ 0 & 0 & 0 & P_{64} & 0 \end{bmatrix},
$$

$$
P_{up2} = \begin{bmatrix} P_{16} & P_{17} & 0 \\ P_{26} & P_{27} & 0 \\ P_{36} & P_{37} & 0 \\ P_{46} & P_{47} & 0 \\ P_{56} & P_{57} & P_{58} \\ P_{66} & P_{67} & P_{68} \end{bmatrix}, \quad P_{lo1} = \begin{bmatrix} 1 & 0 & 0 & 0 & 0 \\ 0 & 1 & 0 & 0 & 0 \\ 0 & 0 & 1 & P_{94} & -1 \end{bmatrix} \text{ and}
$$

$$
P_{lo2} = \begin{bmatrix} P_{76} & P_{77} & 0 \\ P_{86} & P_{87} & 0 \\ P_{96} & P_{97} & P_{98} \end{bmatrix}.
$$

After establishing the generalized system model matrix (P), the next step of H_∞ control problem is to create a closed-loop transfer matrix from the external inputs vector $[v_{xr} \quad v_{yr} \quad v_{zr} \quad z_S \quad n]^T$ to the controlled outputs vector $[y_{x1} \quad y_{x2} \quad y_{y1} \quad y_{y2} \quad y_{z1} \quad y_{z2}]^T$. This closed-loop transfer matrix is generally referred to as a lower *linear fractional transformation* (LFT) and is given by:

$$
F_l(P, K) = P_{up1} + P_{up2}K(I - P_{lo2})^{-1}P_{lo1} \tag{25}
$$

where, K represents the controller dynamics as shown in Fig. 6. The objective of the H_∞ control design is to find a controller (K) which stabilizes the generalized system model (P) and generates the control signal which counteracts the influence of the external inputs vector on the controlled outputs vector by minimizing the H_∞ norm (γ) of the closed-loop transfer matrix $\|F_l(P, K)\|_\infty$. This H_∞ control problem is then solved by the Algebraic Riccati equation approach as presented in [46]. A 22^{nd} order MIMO H_∞ controller is achieved with the value of $\gamma = 0.99$.

The overall closed-loop system will be stable if in H_∞ framework, the closed-loop transfer matrix between the external inputs vector and the controlled outputs vector is internally stable. Lets say, $M = F_l(P, K)$, which has the dimension of (6×5) and can easily be achieved from (25), is given by:

$$
\begin{bmatrix} y_{x1} \\ y_{x2} \\ y_{y1} \\ y_{y2} \\ y_{z1} \\ y_{z2} \end{bmatrix} = \underbrace{F_l(P, K)}_{M} \begin{bmatrix} v_{xr} \\ v_{yr} \\ v_{zr} \\ z_S \\ n \end{bmatrix} \tag{26}
$$

then the condition for the closed-loop internal stability is that all the elements of M are stable. It has been verified that there are no zeros in Re $s \geq 0$ in the characteristic polynomial of each element of M to guarantee the closed-loop internal stability of the system.

V. RESULTS AND DISCUSSION

In order to analyze the performance of the presented control scheme, three different types of scanning trajectories are considered for the horizontal x and y directions: i) *raster scanning* ii) *spiral scanning* and iii) *Lissajous scanning*. The raster scanning is the most conventional scanning method. However, in recent years, the need for higher imaging speeds has motivated the investigation of novel scanning trajectories like spiral scanning and Lissajous scanning.

For the purpose of performance comparison, SISO (Single Input Single Output) H_∞ feedback controller is also designed, individually for each axis, by considering the same performance weighting functions as considered for the design of MIMO H_∞ feedback controller. A 6^{th} order SISO H_∞ feedback controller is achieved for the horizontal x as well as for y directions with $\gamma = 0.89$. For the vertical z-direction, a 6^{th} order SISO H_∞ feedback controller is also designed with $\gamma = 0.72$.

In order to thoroughly analyze the performance of the considered system, three different cases are examined for each different type of scanning trajectory. The considered three cases are:

Case I: SISO H_∞ feedback controller with feedforward compensator *without* cross-couplings.

Case II: SISO H_∞ feedback controller with feedforward compensator *with* cross-couplings.

Case III: MIMO H_∞ feedback controller with feedforward compensator *with* cross-couplings.

All analysis has been done in the presence of nonlinear system model with sensor noise (n) of $10mV/\sqrt{Hz}$ and sample surface variations (sinusoidal) (z_S) of amplitude 0.5 Å with the frequency of 1000 rad/sec.

For each above mentioned case, the tracking performance in horizontal x and y directions is evaluated by calculating the mean-absolute-error (MAE) where error is the difference

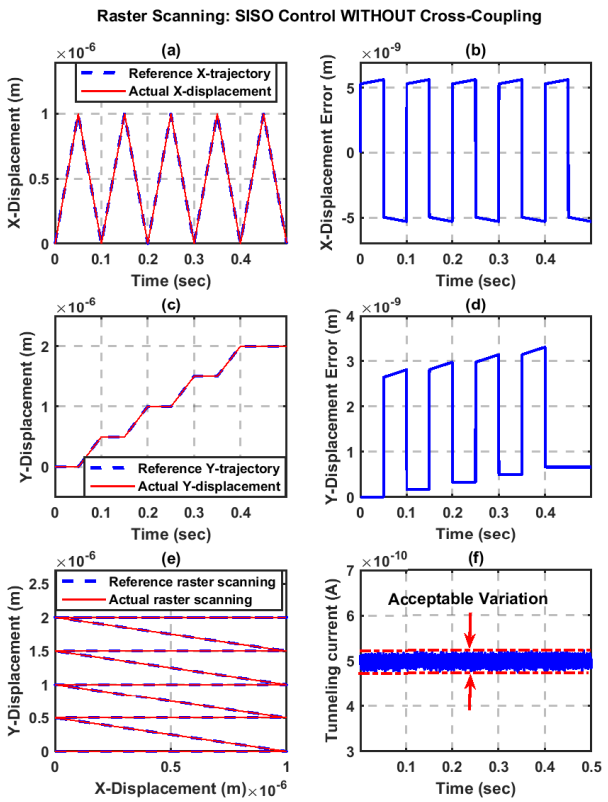

FIGURE 7. Case I with Raster Scanning: SISO H_∞ feedback controllers with feedforward compensators WITHOUT cross-coupling (a)-(b) X-displacement and corresponding error (c)-(d) Y-displacement and corresponding error (e) Reference and actual raster scanning (f) Tunneling current variations.

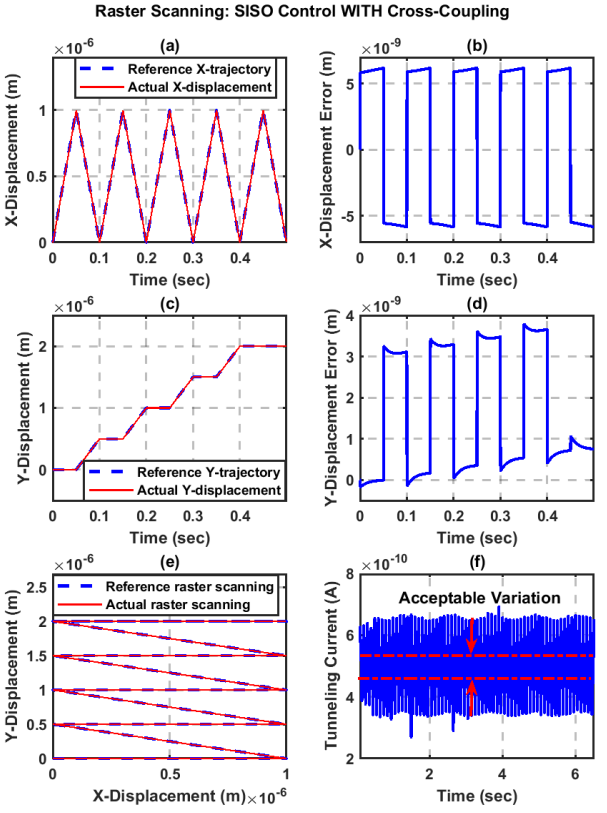

FIGURE 8. Case II with Raster Scanning: SISO H_∞ feedback controllers with feedforward compensators WITH cross-coupling (a)-(b) X-displacement and corresponding error (c)-(d) Y-displacement and corresponding error (e) Reference and actual raster scanning (f) Tunneling current variations.

between the reference trajectory and the actual displacement of the piezoelectric actuator. The mean-absolute-error is calculated as:

$$MAE = \frac{\sum_{a=1}^{N} |R_a - Y_a|}{N} \tag{27}$$

where, R and Y are the reference and the actual displacements of the piezoelectric actuator respectively and N is the total number of data points. In the vertical z-direction, the objective is to maintain the tunneling current constant, while scanning the sample surface, and the performance in each case is evaluated by calculating the standard deviation (SD) of the tunneling current. The standard deviation is calculated as:

$$SD = \sqrt{\frac{1}{N-1} \sum_{a=1}^{N} |i_{Ta} - m|^2} \tag{28}$$

where, i_T is the tunneling current, m is its mean value and N is the total number of data points.

A. RASTER SCANNING

For raster scanning of the sample surface, a triangular waveform is applied to the x-axis and a smooth staircase waveform is applied to the y-axis. The sample surface of the area $1\mu m \times 2\mu m$ is scanned in x and y directions, while keeping the tunneling current constant at $0.5nA$ in the vertical z-direction.

First of all, the analysis is performed with the SISO H_∞ feedback controller cascaded in series with the feedforward compensator without cross-couplings (Case I). It can be observed in Fig. 7 that the precise reference tracking in x and y directions is achieved with the variations of the tunneling current (i_t) remain within the acceptable bound of $\pm 5\%$. The achieved mean absolute errors are 5.23 nm and 1.42 nm in x and y directions respectively. These mean absolute errors are approximately 0.52% and 0.07% of the reference trajectories in x and y directions respectively. The achieved standard deviation of the tunneling current in the vertical z-direction is 7.18 pA. So, the SISO H_∞ feedback controller with the feedforward compensator works well and the desired performance of the system can be achieved if the cross-couplings of the piezoelectric actuator are neglected.

Next, the analysis is performed with the same SISO H_∞ feedback controller cascaded in series with the feedforward compensator in the presence of cross-couplings of the piezoelectric actuator (Case II). A small increase in the tracking errors in the horizontal x and y directions can be observed in Fig. 8 but the tunneling current variations are now large and beyond the acceptable bound of $\pm 5\%$. The achieved

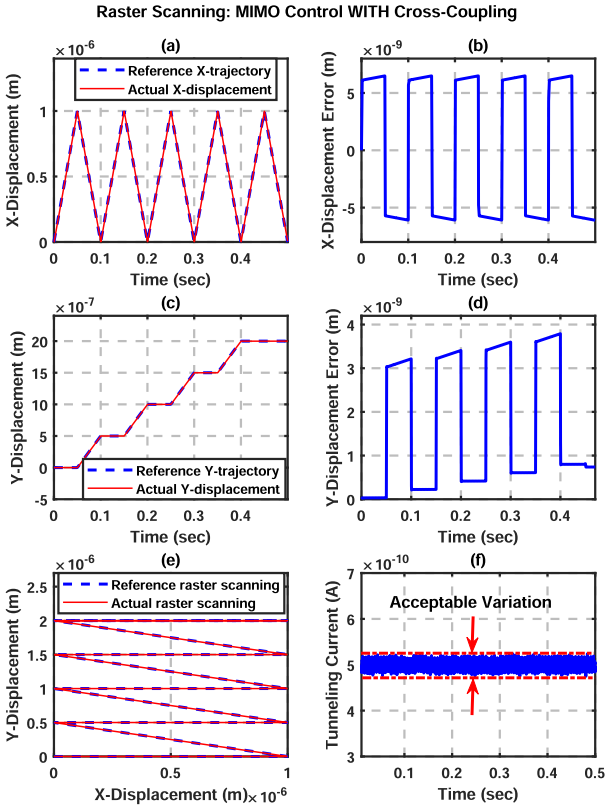

FIGURE 9. Case III with Raster Scanning: MIMO H_∞ feedback controller with feedforward compensators WITH cross-coupling (a)-(b) X-displacement and corresponding error (c)-(d) Y-displacement and corresponding error (e) Reference and actual raster scanning (f) Tunneling current variations.

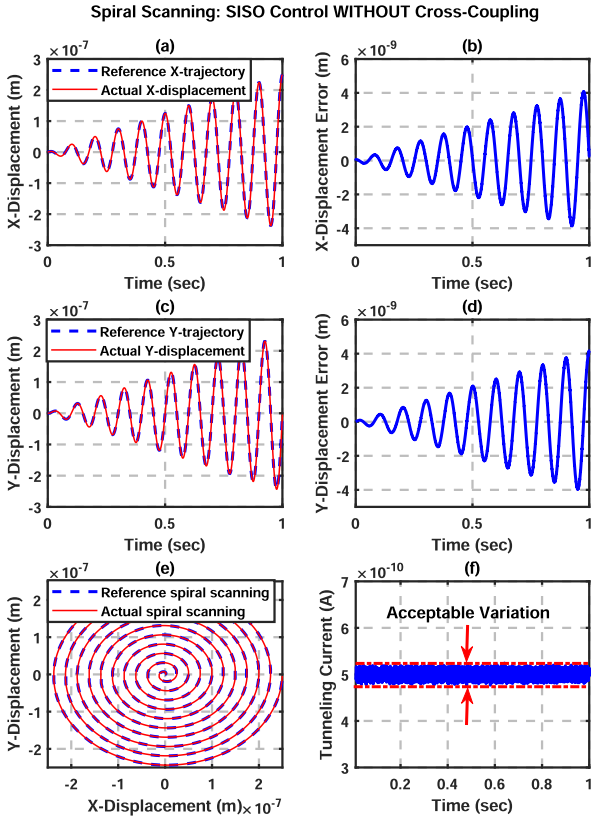

FIGURE 10. Case I with Spiral Scanning: SISO H_∞ feedback controllers with feedforward compensators WITHOUT cross-coupling (a)-(b) X-displacement and corresponding error (c)-(d) Y-displacement and corresponding error (e) Reference and actual spiral scanning (f) Tunneling current variations.

mean absolute errors are 6.31 nm (0.63% of the reference trajectory) and 1.73 nm (0.09% of the reference trajectory) in x and y directions respectively. The standard deviation of the tunneling current is 57.32 pA. This result indicates that the desired performance of the considered system cannot be achieved with SISO control scheme in the presence of cross-couplings.

Finally, the analysis is performed with the suggested MIMO H_∞ feedback controller cascaded in series with the feedforward compensator in the presence of cross couplings (Case III). Fig. 9 shows that the tunneling current variations are now within the acceptable bound of $\pm 5\%$ even in the presence of cross-couplings. The standard deviation of the tunneling current in the vertical z-direction is 7.66 pA and the mean absolute errors in the horizontal x and y directions are 6.07 nm and 1.64 nm respectively. These mean absolute errors are actually 0.61% of the reference trajectory in x-direction and 0.08% in y-direction. All these results indicate that the desired performance of the system can be well achieved with the suggested MIMO H_∞ feedback controller cascaded in series with the feedforward compensator in the presence of cross-couplings. The achieved results in all three cases with the raster scanning are summarized in Table 2.

TABLE 2. Mean Absolute Error (MAE) of tracking in X and Y directions with raster scanning ($1\mu m \times 2\mu m$) and Standard Deviation (STD) of tunneling current in Z direction.

RASTER SCANNING			
Cases	**MAE in X** (nm)	**MAE in Y** (nm)	**STD in Z** (pA)
Case I: SISO control scheme *without* cross-coupling	5.23	1.42	7.18
Case II: SISO control scheme *with* cross-coupling	6.31	1.73	57.32
Case III: MIMO control scheme *with* cross-coupling	6.07	1.64	7.66

B. SPIRAL SCANNING

In spiral scanning, the x and y scan trajectories consist of a sinusoidal and cosine waveform of the same frequency but varying amplitude. For spiral scanning, the sample surface of the area $0.5\mu m \times 0.5\mu m$ is scanned in the horizontal x and y directions, while keeping the tunneling current constant at 0.5 nA in the vertical z direction.

For spiral scanning, first of all, the analysis is performed with the SISO H_∞ feedback controller with feedforward

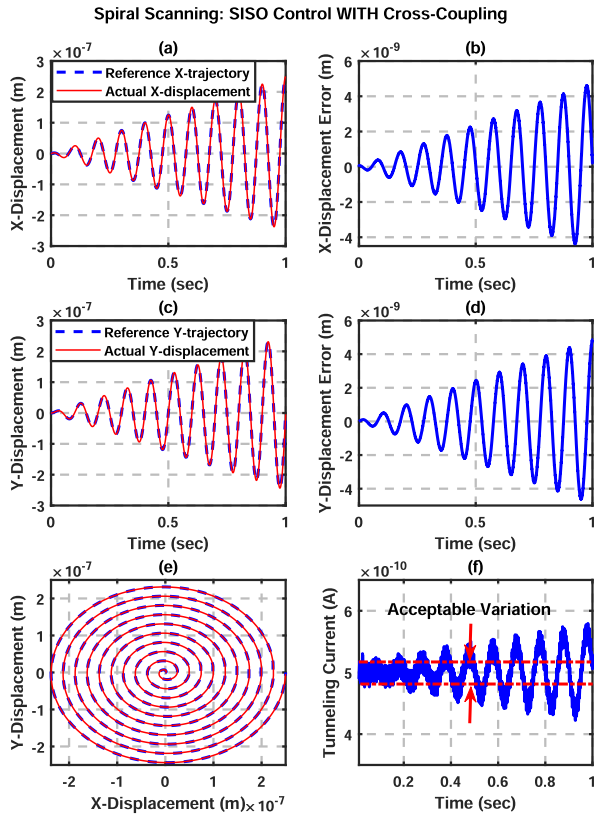

FIGURE 11. Case II with Spiral Scanning: SISO H_∞ feedback controllers with feedforward compensators WITH cross-coupling (a)-(b) X-displacement and corresponding error (c)-(d) Y-displacement and corresponding error (e) Reference and actual spiral scanning (f) Tunneling current variations.

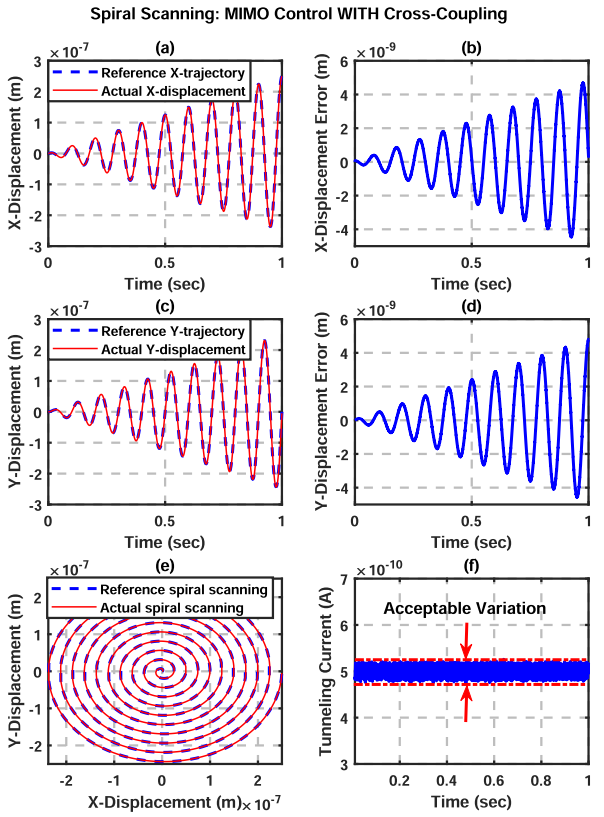

FIGURE 12. Case III with Spiral Scanning: MIMO H_∞ feedback controller with feedforward compensators WITH cross-coupling (a)-(b) X-displacement and corresponding error (c)-(d) Y-displacement and corresponding error (e) Reference and actual spiral scanning (f) Tunneling current variations.

compensator without cross couplings (Case I). The precise reference tracking with the mean absolute errors of 1.33 nm and 1.32 nm in x and y directions respectively can be observed in Fig. 10. These achieved mean absolute errors are actually 0.27% and 0.26% of the reference trajectories in x and y directions respectively. The reference and actual spiral scanning can also be observed in Fig. 10(e). It can also be observed that the variations of the tunneling current remain within the acceptable bound of ±5% with the standard deviation of 6.82 pA in the absence of cross-couplings. So, the desired performance in case of the spiral scanning is well achieved with the SISO control scheme in the absence of cross-couplings.

After the analysis of the SISO control scheme in the absence of cross-coupling, next the analysis is performed with the same SISO control scheme in the presence of cross-couplings (Case II). A small increase in the tracking errors in the horizontal x and y directions can be observed in Fig. 11 as compared to Case I. So, the mean absolute error in x-direction is 1.61 nm (which is 0.32% of the scanning range in x-direction) and in y-direction is 1.56 nm (which is 0.31% of the scanning range in y-direction). In this Case II, a large variations in the tunneling current can be observed and these variations are beyond the acceptable bound of ±5%. The achieved standard deviation of the tunneling current is now 27.73 pA in the presence of cross-couplings. These results indicate that the SISO control scheme will not perform as desired in the presence of cross-couplings.

Finally, the analysis is performed with the suggested MIMO control scheme in the presence of cross-couplings (Case III). Precise reference tracking in the x and y directions with the tunneling current variations within the acceptable bound of ±5% can be observed in Fig. 12. The mean absolute errors in the x and y directions are 1.51 nm and 1.49 nm respectively with the standard deviation of the tunneling current in the vertical z-direction is 7.62 pA. The mean absolute errors are actually 0.3% and 0.29% of the reference trajectories in the x and y directions respectively. All these results indicate that the desired performance is well achieved with the suggested MIMO feedback with feedforward control scheme in the presence of cross-couplings. The achieved results with the spiral scanning are summarized in Table 3.

C. LISSAJOUS SCANNING

In Lissajous scanning, the x and y scan trajectories consist of purely sinusoidal signals that contain slightly different frequencies. The sample surface area of $1\mu m \times 1\mu m$ is scanned in the horizontal x and y directions, while keeping the tunneling current constant at 0.5 nA in the vertical z direction.

TABLE 3. Mean Absolute Error (MAE) of tracking in X and Y directions with spiral scanning ($0.5\mu m \times 0.5\mu m$) and Standard Deviation (STD) of tunneling current in Z direction.

SPIRAL SCANNING			
Cases	**MAE in X** (nm)	**MAE in Y** (nm)	**STD in Z** (pA)
Case I: SISO control scheme *without* cross-coupling	1.33	1.32	6.82
Case II: SISO control scheme *with* cross-coupling	1.61	1.56	27.73
Case III: MIMO control scheme *with* cross-coupling	1.51	1.49	7.62

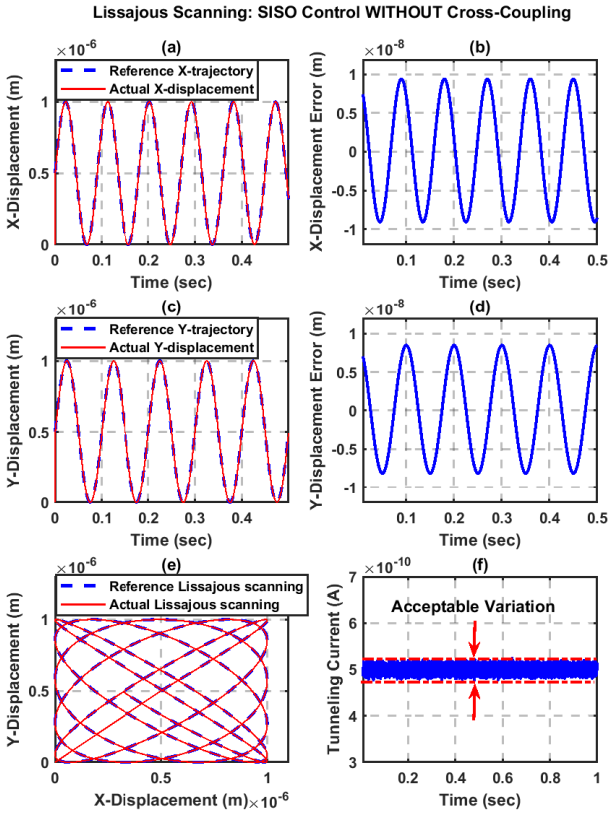

FIGURE 13. Case I with Lissajous Scanning: SISO H_∞ feedback controllers with feedforward compensators WITHOUT cross-coupling (a)-(b) X-displacement and corresponding error (c)-(d) Y-displacement and corresponding error (e) Reference and actual Lissajous scanning (f) Tunneling current variations.

The Lissajous scanning is first performed with the SISO H_∞ feedback controller cascaded in series with the feedforward compensator without cross-couplings (Case I). The precise reference tracking in x and y directions with reference and actual trajectories of Lissajous scanning can be observed in Fig. 13. It can also be observed in Fig. 13 that the tunneling current variations remain within the acceptable bound of $\pm 5\%$ in the absence of cross-couplings. The mean absolute errors of the reference tracking in x and y directions

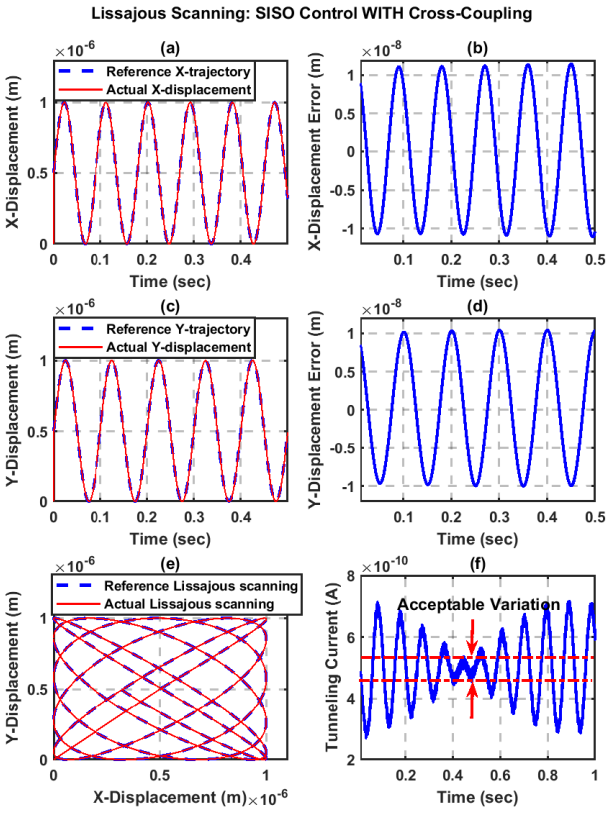

FIGURE 14. Case II with Lissajous Scanning: SISO H_∞ feedback controllers with feedforward compensators WITH cross-coupling (a)-(b) X-displacement and corresponding error (c)-(d) Y-displacement and corresponding error (e) Reference and actual Lissajous scanning (f) Tunneling current variations.

are 5.92 nm (0.59% of the reference trajectory) and 5.29 nm (0.53% of the reference trajectory) respectively. The standard deviation of the tunneling current is 6.92 pA. All these results indicate that the desired performance is well achieved with the SISO control scheme in the absence of cross-couplings.

Next, the analysis is performed with the same SISO H_∞ feedback controller with feedforward compensator in the presence of cross-couplings (Case II). It can be observed in Fig. 14 that the tracking error is now a little increased both in x and y directions. The mean absolute errors of tracking are now 7.03 nm (0.7% of the reference trajectory) and 6.42 nm (0.64% of the reference trajectory) in x and y directions respectively. A large variations in the tunneling current can also be observed in this Fig. 14(f) which indicate that the desired performance specifications cannot be achieved in the presence of cross-couplings with the SISO control scheme. The standard deviation of the tunneling current is now 76.57 pA.

Finally, the analysis is performed for Lissajous scanning with the suggested MIMO H_∞ feedback controller cascaded in series with the feedforward compensator in the presence of cross-couplings (Case III). As compared to Case II, less tracking errors in x and y directions with acceptable variations of the tunneling current can be observed in Case III as

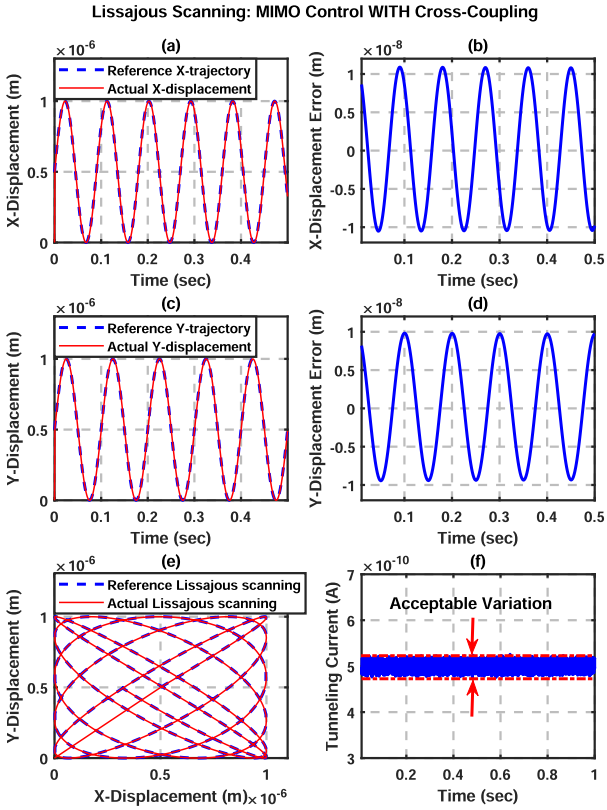

FIGURE 15. Case III with Lissajous Scanning: MIMO H_∞ feedback controller with feedforward compensators WITH cross-coupling (a)-(b) X-displacement and corresponding error (c)-(d) Y-displacement and corresponding error (e) Reference and actual Lissajous scanning (f) Tunneling current variations.

TABLE 4. Mean Absolute Error (MAE) of tracking in X and Y directions with Lissajous scanning ($1\mu m \times 1\mu m$) and Standard Deviation (STD) of tunneling current in Z direction.

LISSAJOUS SCANNING			
Cases	**MAE in X** (nm)	**MAE in Y** (nm)	**STD in Z** (pA)
Case I: SISO control scheme *without* cross-coupling	5.92	5.29	6.92
Case II: SISO control scheme *with* cross-coupling	7.03	6.42	76.57
Case III: MIMO control scheme *with* cross-coupling	6.77	6.12	7.67

shown in Fig. 15. The means absolute errors of tracking are now 6.77 nm (0.68% of the reference trajectory) and 6.12 nm (0.61% of the reference trajectory) in x and y directions respectively. The standard deviation of the tunneling current in the vertical z direction is now 7.67 pA. All these results with Lissajous scanning are summarized in Table 4. It is obvious from the achieved results in Case III that the desired performance of STM is well achieved with the suggested MIMO control scheme in the presence of cross-couplings.

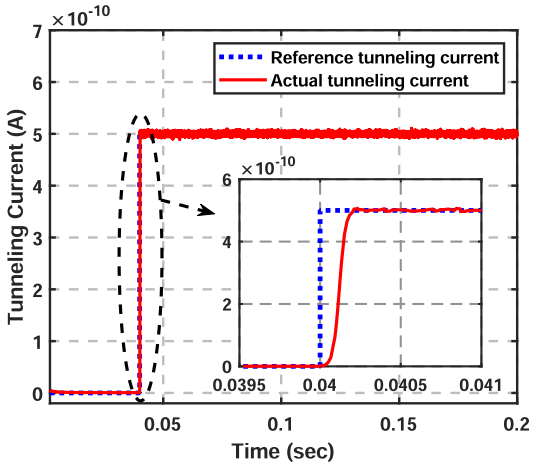

FIGURE 16. Step response of the tunneling current with MIMO H_∞ feedback controller cascaded in series with the feedforward compensator in the presence of cross-coupling to analyze the transient characteristics.

D. TRANSIENT RESPONSE OF TUNNELING CURRENT

The transient characteristics of the tunneling current are important to analyze in order to see how fast the STM tip moves in the tunneling region ($0.1 - 1 \times 10^{-9}$m distance between the tip and the sample surface) and if there is an overshoot whenever there is a change in the reference tunneling current. Ideally, the STM tip must move very fast (settling time less than 1×10^{-3}sec.) in the tunneling region to keep the distance between the tip and the sample surface constant or in other words, to keep the tunneling current constant. Other than this, ideally the overshoot must be reduced (overshoot of 5%) in order to avoid any collision between the sharp metallic tip and the sample surface.

A step response of the tunneling current with the suggested MIMO H_∞ feedback controller cascaded in series with the feedforward compensator in the presence of cross-couplings is presented in Fig. 16 to analyze the transient characteristics. It can be observed in Fig. 16 that the settling time of the system is around 0.2×10^{-3} sec. and the overshoot is almost 0%. This result indicates that a good transient performance is achieved with the suggested feedback - feedforward control scheme.

VI. CONCLUSION

In this paper, the performance of STM having a multi-axis 3D piezoelectric actuator in the presence of two control strategies (SISO and MIMO H_∞ feedback controllers cascaded in series with a feedforward compensator) is thoroughly analyzed. For controller design, a complete MIMO system is mathematically modeled in the presence of cross-couplings as well as hysteresis nonlinearity of the piezoelectric actuator. The parameters of the hysteresis model are identified from the real-time experimental data and the feedforward compensator is designed without calculating the inverse hysteresis model. Three different types of scanning trajectories (raster, spiral and Lissajous) are used for the performance comparison.

It is evident from the achieved results that in the presence of cross-couplings, the SISO control scheme cannot deliver the desired performance. A small increase in the tracking error for horizontal 2D scanning system is observed with SISO control scheme, however, the main issue is the large variations in the tunneling current (beyond the acceptable bound of $\pm 5\%$) due to cross-couplings. These large variations in the tunneling current will result in a surface image that will not correspond to the reality. This issue has been resolved by the suggested MIMO control scheme. In case of the raster scanning, 86.6% improvement is observed in reducing the variations of the tunneling current with the suggested MIMO control scheme in the presence of cross-couplings, 72.5% in case of spiral scanning and 90% in case of Lissajous scanning as compared to the tunneling current variations with the generally used SISO control scheme for STM. All the presented results with different scanning trajectories indicate the efficacy of the suggested MIMO H_∞ feedback controller cascaded in series with the feedforward compensator.

It will be an interesting study in the prospective of the presented work to analyze the performance of the system by considering all the possible adverse effects of a piezoelectric actuator, like creep, hysteresis, high frequency vibrations and cross-couplings altogether with a suitable control methodology.

ACKNOWLEDGMENT

The authors of this paper gratefully acknowledge the technical and financial support of the Researchers Supporting Project (RSP-2021/270), King Saud University, Riyadh, Saudi Arabia.

REFERENCES

[1] G. Binnig and H. Rohrer, "Scanning tunneling microscopy," *Surf. Sci.*, vol. 126, pp. 236–244, Mar. 1983.

[2] M. Razavy, *Quantum Theory of Tunneling*. Singapore: World Scientific, 2013.

[3] B. Yang, B. Wang, H. Yan, and X. Gao, "Design of a micromachined Z-axis tunneling magnetoresistive accelerometer with electrostatic force feedback," *Micromachines*, vol. 10, no. 2, p. 158, Feb. 2019.

[4] M. Denisenko, B. Konoplev, A. Isaeva, and I. Lysenko, "Integrated micromechanical tunneling accelerometer," *J. Pharmaceutical Sci. Res.*, vol. 9, no. 11, pp. 2155–2158, 2017.

[5] M. F. Bocko, "The scanning tunneling microscope as a high-gain, low-noise displacement sensor," *Rev. Sci. Instrum.*, vol. 61, no. 12, pp. 3763–3768, Dec. 1990.

[6] T. W. Kenny, W. J. Kaiser, S. B. Waltman, and J. K. Reynolds, "Novel infrared detector based on a tunneling displacement transducer," *Appl. Phys. Lett.*, vol. 59, no. 15, pp. 1820–1822, Oct. 1991.

[7] S. Devasia, E. Eleftheriou, and S. O. R. Moheimani, "A survey of control issues in nanopositioning," *IEEE Trans. Control Syst. Technol.*, vol. 15, no. 5, pp. 802–823, Sep. 2007.

[8] E. Anguiano, A. I. Oliva, and M. Aguilar, "Optimal conditions for imaging in scanning tunneling microscopy: Theory," *Rev. Sci. Instrum.*, vol. 69, no. 11, pp. 3867–3874, Nov. 1998.

[9] Y. Jian, D. Huang, J. Liu, and D. Min, "High-precision tracking of piezoelectric actuator using iterative learning control and direct inverse compensation of hysteresis," *IEEE Trans. Ind. Electron.*, vol. 66, no. 1, pp. 368–377, Jan. 2019.

[10] P.-B. Nguyen, S.-B. Choi, and B.-K. Song, "A new approach to hysteresis modelling for a piezoelectric actuator using Preisach model and recursive method with an application to open-loop position tracking control," *Sens. Actuators A, Phys.*, vol. 270, no. 1, pp. 136–152, 2017.

[11] M. S. Rana, H. R. Pota, and I. R. Petersen, "A survey of methods used to control piezoelectric tube scanners in high-speed AFM imaging," *Asian J. Control*, vol. 20, no. 4, pp. 1379–1399, Jul. 2018.

[12] Z. Wu, M. Chen, P. He, H. Li, Q. Zhang, X. Xiong, H.-Y. Mi, Z. Li, and Y. Li, "Tracking control of PZT-driven compliant precision positioning micromanipulator," *IEEE Access*, vol. 8, pp. 126477–126487, 2020.

[13] G.-Y. Gu, L.-M. Zhu, C.-Y. Su, H. Ding, and S. Fatikow, "Modeling and control of piezo-actuated nanopositioning stages: A survey," *IEEE Trans. Autom. Sci. Eng.*, vol. 13, no. 1, pp. 313–332, Jan. 2016.

[14] M. Al Janaideh, M. Al Saaideh, and M. Rakotondrabe, "On hysteresis modeling of a piezoelectric precise positioning system under variable temperature," *Mech. Syst. Signal Process.*, vol. 145, Nov. 2020, Art. no. 106880.

[15] Y. Qin, X. Zhao, and L. Zhou, "Modeling and identification of the rate-dependent hysteresis of piezoelectric actuator using a modified Prandtl–Ishlinskii model," *Micromachines*, vol. 8, no. 4, p. 114, Apr. 2017.

[16] N. N. Son, C. Van Kien, and H. P. H. Anh, "Parameters identification of Bouc–Wen hysteresis model for piezoelectric actuators using hybrid adaptive differential evolution and Jaya algorithm," *Eng. Appl. Artif. Intell.*, vol. 87, Jan. 2020, Art. no. 103317.

[17] J. Gan, Z. Mei, X. Chen, Y. Zhou, and M. F. Ge, "A modified Duhem model for rate-dependent hysteresis behaviors," *Micromachines*, vol. 10, no. 10, p. 680, Oct. 2019.

[18] R. Xu, X. Zhang, H. Guo, and M. Zhou, "Sliding mode tracking control with perturbation estimation for hysteresis nonlinearity of piezo-actuated stages," *IEEE Access*, vol. 6, pp. 30617–30629, 2018.

[19] I. Ahmad, M. A. Ali, and W. Ko, "Robust μ-synthesis with Dahl model based feedforward compensator design for piezo-actuated micropositioning stage," *IEEE Access*, vol. 8, pp. 141799–141813, 2020.

[20] D. Meng, P. Xia, K. Lang, E. C. Smith, and C. D. Rahn, "Neural network based hysteresis compensation of piezoelectric stack actuator driven active control of helicopter vibration," *Sens. Actuators A, Phys.*, vol. 302, Feb. 2020, Art. no. 111809.

[21] Y.-R. Ko, Y. Hwang, M. Chae, and T.-H. Kim, "Direct identification of generalized Prandtl–Ishlinskii model inversion for asymmetric hysteresis compensation," *ISA Trans.*, vol. 70, pp. 209–218, Sep. 2017.

[22] I. Ahmad, "Two degree-of-freedom robust digital controller design with Bouc–Wen hysteresis compensator for piezoelectric positioning stage," *IEEE Access*, vol. 6, pp. 17275–17283, 2018.

[23] J. Gan and X. Zhang, "A review of nonlinear hysteresis modeling and control of piezoelectric actuators," *AIP Adv.*, vol. 9, no. 4, Apr. 2019, Art. no. 040702.

[24] D. V. Sabarianand, P. Karthikeyan, and T. Muthuramalingam, "A review on control strategies for compensation of hysteresis and creep on piezoelectric actuators based micro systems," *Mech. Syst. Signal Process.*, vol. 140, Jun. 2020, Art. no. 106634.

[25] H. Jung, J. Y. Shim, and D. Gweon, "New open-loop actuating method of piezoelectric actuators for removing hysteresis and creep," *Rev. Sci. Instrum.*, vol. 71, no. 9, pp. 3436–3440, Sep. 2000.

[26] Y. Liu, J. Shan, and N. Qi, "Creep modeling and identification for piezoelectric actuators based on fractional-order system," *Mechatronics*, vol. 23, no. 7, pp. 840–847, Oct. 2013.

[27] B. J. G. Vautier and S. Moheimani, "Charge driven piezoelectric actuators for structural vibration control: Issues and implementation," *Smart Mater. Struct.*, vol. 14, no. 4, p. 575, 2005.

[28] H. Habibullah, "30 years of atomic force microscopy: Creep, hysteresis, cross-coupling, and vibration problems of piezoelectric tube scanners," *Measurement*, vol. 159, Jul. 2020, Art. no. 107776.

[29] S. Li, P. He, S. K. Nguang, and X. Lin, "Barrier function-based adaptive neuro network sliding mode vibration control for flexible double-clamped beams with input saturation," *IEEE Access*, vol. 8, pp. 125887–125898, 2020.

[30] A. I. Oliva, E. Anguiano, N. Denisenko, M. Aguilar, and J. L. Peña, "Analysis of scanning tunneling microscopy feedback system," *Rev. Sci. Instrum.*, vol. 66, no. 5, pp. 3196–3203, May 1995.

[31] E. Anguiano, A. I. Oliva, M. Aguilar, and J. L. Peña, "Analysis of scanning tunneling microscopy feedback system: Experimental determination of parameters," *Rev. Sci. Instrum.*, vol. 67, no. 8, pp. 2947–2952, Aug. 1996.

[32] F. Tajaddodianfar, S. O. R. Moheimani, and J. N. Randall, "Scanning tunneling microscope control: A self-tuning PI controller based on online local barrier height estimation," *IEEE Trans. Control Syst. Technol.*, vol. 27, no. 5, pp. 2004–2015, Sep. 2019.

[33] F. Tajaddodianfar, S. O. R. Moheimani, E. Fuchs, and J. N. Randall, "Stability analysis of a scanning tunneling microscope control system," in *Proc. Amer. Control Conf. (ACC)*, May 2017, pp. 204–209.
[34] N. Bonnail, D. Tonneau, F. Jandard, G. A. Capolino, and H. Dallaporta, "Variable structure control of a piezoelectric actuator for a scanning tunneling microscope," *IEEE Trans. Ind. Electron.*, vol. 51, no. 2, pp. 354–363, Apr. 2004.
[35] S. Tien, Q. Zou, and S. Devasia, "Iterative control of dynamics-coupling effects in piezo-based nano-positioners for high-speed AFM," in *Proc. IEEE Int. Conf. Control Appl.*, Sep. 2004, pp. 711–717.
[36] Y. Wu, J. Shi, C. Su, and Q. Zou, "A control approach to cross-coupling compensation of piezotube scanners in tapping-mode atomic force microscope imaging," *Rev. Sci. Instrum.*, vol. 80, no. 4, Apr. 2009, Art. no. 043709.
[37] Y. K. Yong, K. Liu, and S. O. R. Moheimani, "Reducing cross-coupling in a compliant XY nanopositioner for fast and accurate raster scanning," *IEEE Trans. Control Syst. Technol.*, vol. 18, no. 5, pp. 1172–1179, Sep. 2010.
[38] L. Li, C.-X. Li, G. Gu, and L. Zhu, "Modified repetitive control based cross-coupling compensation approach for the piezoelectric tube scanner of atomic force microscopes," *IEEE/ASME Trans. Mechatronics*, vol. 24, no. 2, pp. 666–676, Apr. 2019.
[39] H. R. Pota, I. R. Petersen, and M. S. Rana, "Creep, hysteresis, and cross-coupling reduction in the high-precision positioning of the piezoelectric scanner stage of an atomic force microscope," *IEEE Trans. Nanotechnol.*, vol. 12, no. 6, pp. 1125–1134, Sep. 2013.
[40] L. Ryba, A. Voda, and G. Besancon, "Modelling and control of 3D STM-like scanning device with application to surface reconstruction," in *Proc. 18th Int. Conf. Methods Models Autom. Robot. (MMAR)*, Aug. 2013, pp. 479–484.
[41] D. Habineza, M. Zouari, Y. Le Gorrec, and M. Rakotondrabe, "Multivariable compensation of hysteresis, creep, badly damped vibration, and cross couplings in multiaxes piezoelectric actuators," *IEEE Trans. Autom. Sci. Eng.*, vol. 15, no. 4, pp. 1639–1653, Oct. 2018.
[42] M. Ismail, F. Ikhouane, and J. Rodellar, "The hysteresis Bouc–Wen model, a survey," *Arch. Comput. Methods Eng.*, vol. 16, no. 2, pp. 161–188, 2009.
[43] M. Ming, Z. Feng, J. Ling, and X. Xiao, "Hysteresis modelling and feedforward compensation of piezoelectric nanopositioning stage with a modified Bouc–Wen model," *Micro Nano Lett.*, vol. 13, no. 8, pp. 1170–1174, Aug. 2018.
[44] A. Shafiee, A. Ahmadian, and A. Akbari, "A parametric study of mechanical cross-coupling in parallel-kinematics piezo-flexural nano-positioning systems," *Open J. Appl. Sci.*, vol. 11, no. 5, pp. 596–613, 2021.
[45] M. Rakotondrabe, "Bouc–Wen modeling and inverse multiplicative structure to compensate hysteresis nonlinearity in piezoelectric actuators," *IEEE Trans. Autom. Sci. Eng.*, vol. 8, no. 2, pp. 428–431, Apr. 2011.
[46] S. Skogestad and I. Postlethwaite, *Multivariable Feedback Control: Analysis and Design*, vol. 2. Princeton, NJ, USA: Citeseer, 2007.

IRFAN AHMAD received the M.S. and Ph.D. degrees in control systems from the University of Grenoble (Grenoble Institute of Technology), France, in 2007 and 2011, respectively.

He was worked as a Research and Teaching Assistant with the GIPSA-Laboratory and Polytech Grenoble, University of Joseph Fourier, Grenoble, France, from 2010 to 2011, and then with the Laboratoire de Conception et d'Intégration des Systèmes (LCIS) and ESISAR, Valence, France, from 2011 to 2012. He is currently working as an Assistant Professor with the Electrical Engineering Department, King Saud University, Riyadh, KSA. His current research interests include optimal and robust control design for MEMS/NEMS technology and for other different applications.

AMRO EMAD AWAD ALI received the B.Sc. degree in electrical engineering with specialty of control systems from the Sudan University of Science and Technology (SUST), Khartoum, Sudan, in 2014. He is currently pursuing the M.Sc. degree in electrical engineering with specialty of computer and control systems with the Electrical Engineering Department, King Saud University, Riyadh, KSA. He worked as a Teaching Assistant with SUST, from 2014 to 2016, and then as an Instruments and Control Engineer with Sudanese Thermal Power Generating Company Ltd. (STPG), from 2016 to 2018. His research interests include system identification and robust control design for micro/nanotechnology and renewable energy.

YASSER BIN SALAMAH received the M.S. and Ph.D. degrees from The Ohio State University (OSU), Columbus, OH, USA, in 2013 and 2019, respectively. He is currently an Assistant Professor in electrical engineering with King Saud University, Riyadh, Saudi Arabia. His research interests include optimization, intelligent control, artificial intelligence with application to autonomous systems, and renewable energy.